Towards Binary Gas Mixture ZDES for Space Launcher Base Flow Prediction

Jolan Reynaud, Pierre-Elie Weiss, Sébastien Deck

▶ **To cite this version:**

Jolan Reynaud, Pierre-Elie Weiss, Sébastien Deck. Towards Binary Gas Mixture ZDES for Space Launcher Base Flow Prediction. 55th 3AF International Conference on Applied Aerodynamics, Apr 2021, Poitiers, France. hal-03227829

HAL Id: hal-03227829
https://hal.science/hal-03227829v1

Submitted on 17 May 2021

HAL is a multi-disciplinary open access archive for the deposit and dissemination of scientific research documents, whether they are published or not. The documents may come from teaching and research institutions in France or abroad, or from public or private research centers.

L'archive ouverte pluridisciplinaire **HAL**, est destinée au dépôt et à la diffusion de documents scientifiques de niveau recherche, publiés ou non, émanant des établissements d'enseignement et de recherche français ou étrangers, des laboratoires publics ou privés.

Association Aéronautique et Astronautique de France

55th 3AF International Conference on Applied Aerodynamics
Virtual Conference - April 12-13-14, 2021

FP13-AERO2020-reynaud

Towards Binary Gas Mixture ZDES for Space Launcher Base Flow Prediction

J.Reynaud[(1)], P-E.Weiss, [(1)] and S.Deck[(1)]

[(1)]ONERA-The French Aerospace Lab, 8 rue des Vertugadins 92190 Meudon (France), pierre-elie.weiss@onera.fr

ABSTRACT

In order to improve space launcher base flow predictions, it has been shown that the thermodynamic properties of the propulsive jet had to be taken into account. To this end, this paper proposes an extension of a mono-species Navier-Stokes solver (FLU3M) to permit the simulation of inert bi-species flows. The extended framework is based on a six-equation finite volume formulation. The physical modelling and the different numerical methods implemented are first described and then validated on a set of test cases of growing complexity with successful RANS and ZDES bi-species simulations. The framework is then used to study a generic space launcher base flow.

1. INTRODUCTION

The prediction of the afterbody flow of a space launcher during its flight is of primary importance for the correct assessment of the aerodynamic performance and the stability of the vehicle, especially in order to establish new designs such as reusable launchers. In flight, the massively separated turbulent flow behind the base and around the nozzle(s) induces two major effects: base drag and side-loads. First, base drag, mainly due to the low pressure recirculation zone forming behind the base constitutes a significant contribution to the overall drag. Then, side-loads (related to the buffeting phenomena), caused by pressure fluctuations linked to the large-scale unsteady motion of the recirculation bubble, influence the flight stability and may cause vibrations of the mechanical structures. The multi-gas interactions between the propulsive jet(s) and the base flow may furthermore enhance the adverse effects. Extrapolations of air-only simulation results to real flight conditions are known to be limited [15] and physical properties of the exhaust gas have thus to be taken into account for realistic predictions.

As a result of this complexity, performing an accurate simulation of a launcher's aerodynamics in flight-like conditions remains a challenge for wind tunnel testing [25] (scaling issues, measurements limitations, probe integrity, exploitation costs) and computational fluid dynamics [4] (turbulence modelling, numerical accuracy, multi-physics coupling, computational costs). The aerodynamic design of space launchers is thus still largely based on semi-empirical methods. To contribute to the progress in space launcher base flow predictions, we propose an extension of the Navier-Stokes solver FLU3M (widely used on space launcher cases for mono-species simulations [20]) to enable the simulation of turbulent flows containing two inert and calorically perfect gases. A pre-existing explicit, Euler bi-species module [13] is the basis of our numerical framework. This new framework, enabling to define different gas properties for the outer flow and the exhaust gas, could represent a good compromise between modelling complexity and relevant physics prediction for space launcher aerodynamics. The paper focuses on the extension of the solver and its validation test cases of growing complexity. An application on a generic launcher design is then presented.

2. PHYSICAL MODELLING

2.1 Governing equations

To describe a binary gas mixture flow (no source terms), one can use the general conservative form of the averaged or filtered Navier Stokes equations:

$$\frac{\partial \mathbf{w}_c}{\partial t} + div(\mathscr{F}) = div(\mathscr{G}) \tag{1}$$

$\mathbf{w}_c =^t (\rho_1, \rho_2{}^1, \rho\mathbf{V}, \rho E)$ denotes the vector of conserved quantities, containing 6 variables against 5 in a mono-species case. ρ_1 et ρ_2 are the two gas densities and ρ is the density of the mixture. $\mathbf{V} =^t (u, v, w)$ is the velocity

[1]The blue terms represent the difference between a mono-species formulation and a two-species one.

vector of the flow and E is the total energy of the mixture. $\mathscr{F}$ and $\mathscr{G}$ are the convection and diffusion terms:

$$\mathscr{F} =^t (\rho_1 \mathbf{V}, \rho_2 \mathbf{V}, \rho \mathbf{V} \otimes \mathbf{V} + p\bar{\bar{I}}, (\rho E + p)\mathbf{V}) \quad (2)$$

$$\mathscr{G} =^t (\mathbf{J}_1^*, \mathbf{J}_2^*, \bar{\bar{\tau}}^*, \bar{\bar{\tau}}^*.\mathbf{V} - \mathbf{q}^* - \mathbf{J}_E^*) \quad (3)$$

With P the mixture pressure, $\mathbf{J}_i^* = \mathbf{J}_i + \mathbf{J}_{t_i}$ the total mass flux of the ith species with $\mathbf{J}_i$ the laminar mass flux and $\mathbf{J}_{t_i}$ the unresolved turbulent mass flux , $\mathbf{q}^* = \mathbf{q} + \mathbf{q}_t$ the total heat flux with $\mathbf{q}$ the laminar heat flux and $\mathbf{q}_t$ the unresolved turbulent heat flux, $\mathbf{J}_E^*$ the total energy flux. $\bar{\bar{\tau}}^*$ is the combination of the viscous stress and the unresovled turbulent stress tensors:

$$\tau_{ij}^* = 2(\mu + \mu_t)(S_{ij} - \frac{1}{3}\delta_{ij}S_{ii}) \qquad i,j = 1..3 \quad (4)$$

$$S_{ij} = \frac{1}{2}(\frac{\partial u_i}{\partial x_j} + \frac{\partial u_j}{\partial x_i}) \qquad i,j = 1..3 \quad (5)$$

with μ and μ_t being the dynamic viscosity and the turbulent viscosity which is provided by a turbulence model. In this study we will use the Spalart-Allmaras [28] RANS approach and the ZDES multi-resolution approach [9].

2.2 Thermodynamic Properties

Several equations describing the thermodynamic properties of the two calorically perfect gases and the transport properties of the flow are needed to close the governing equations. First, in any volume, the density of the mixture is defined as :

$$\rho = \rho_1 + \rho_2 = \rho(Y_1 + Y_2) \quad (6)$$

with Y_i the mass fraction of the ith species. As a consequence of this definition we can note that :

$$\boxed{Y_1 + Y_2 = 1 \quad and \quad \nabla Y_1 = -\nabla Y_2} \quad (7)$$

The thermodynamic properties for each of the two gases (i=1,2) are defined as :

$$\gamma_i = \frac{c_{p_i}}{c_{v_i}}, \quad c_{p_i} - c_{v_i} = r_i \quad (8)$$

c_{p_i} et c_{v_i} being the constant pressure and the constant volume heat capacities , γ_i the specific heat ratio and r_i the specific gas constant. Assuming a thermal equilibrium between the two gases, we define the internal energy e_i and the specific enthalpy h_i :

$$e_i = c_{v_i}T \quad , \quad h_i = c_{p_i}T = \gamma_i e_i = e_i + \frac{p_i}{\rho_i} \quad (9)$$

As these quantities are extensive, one can deduce:

$$c_v = Y_1 c_{v_1} + Y_2 c_{v_2}, \quad c_p = Y_1 c_{p_1} + Y_2 c_{p_2} \quad (10)$$

$$\gamma = \frac{c_p}{c_v} = \frac{Y_1\gamma_1 c_{v_1} + Y_2\gamma_2 c_{v_2}}{Y_1 c_{v_1} + Y_2 c_{v_2}}, \quad r = c_p - c_v = Y_1 r_1 + Y_2 r_2 \quad (11)$$

Then, using the Dalton's Law for calorically perfect gases, the mixture pressure is obtained as the sum of both partial pressures to express the equation of state for the mixture. Finally, internal energy and pressure are coupled and the total energy of the mixture is expressed as follows :

$$p = p_1 + p_2 = (\rho_1 r_1 + \rho_2 r_2)T = \rho r T \quad (12)$$

$$p = \rho r \frac{e}{c_v} = \rho(\gamma - 1)e, \quad \rho E = \rho e + \frac{1}{2}\rho \mathbf{V}^2 \quad (13)$$

2.3 Transport Properties

Viscous Flux An acknowledged approximation for binary gas mixture is to define the viscosity as a weighted sum of the two species viscosity [26] :

$$\mu = Y_1\mu_1 + Y_2\mu_2 \quad (14)$$

For each species, the viscosity μ_i is given by a Sutherland's law. The total viscosity can thus be defined as $\mu^* = \mu + \mu_t$.

Energy Flux The heat flux $\mathbf{q}$ from Fourier's law is:

$$\mathbf{q} = -\lambda \nabla T \quad (15)$$

We define the thermal conductivity for each species thanks to a constant Prandtl number Pr_i. The thermal conductivity of the mixture is then estimated as a viscosity-weighted average of both conductivities [26]:

$$\lambda_i = \frac{\mu_i c_{p_i}}{Pr_i}, \quad \lambda = \mu(\frac{\lambda_1}{\mu_1}Y_1 + \frac{\lambda_2}{\mu_2}Y_2) \quad (16)$$

To account for the effect of turbulence on heat transfer, the turbulent heat flux $\mathbf{q}_t$ is defined thanks to a turbulent Prandtl number defined for the mixture flow:

$$\mathbf{q}_t = -\lambda_t \nabla T, \quad \lambda_t = \frac{\mu_t c_p}{Pr_t} \quad (17)$$

The total thermal conductivity is then defined as $\boxed{\lambda^* = \lambda + \lambda_t}$. Moreover, in a mixture, the energy flux is linked to the diffusion of enthalpy:

$$\mathbf{J}_E^* = \mathbf{J}_1^* h_1 + \mathbf{J}_2^* h_2 \quad (18)$$

Mass Diffusion To model mass diffusion fluxes, the Hirschfelder-Curtis approximation [16] is considered as the most accurate first order approximation available. For a binary gas mixture, it reduces to Fick's diffusion law [23]:

$$\boxed{\mathbf{J}_1 = -\rho D \nabla Y_1} \quad \boxed{\mathbf{J}_2 = -\rho D \nabla Y_2} \quad (19)$$

With D=$\mathscr{D}_{12} = \mathscr{D}_{21}$ the mixture diffusion coefficient. This formulation traduces the tendency to balance mass fractions as the fluxes are opposed to mass fraction gradients. The mass conservation condition can be verified:

$$\mathbf{J}_1 + \mathbf{J}_2 = -\rho D(\nabla Y_1 + \nabla Y_2) = 0 \tag{20}$$

The diffusion coefficient D may be derived from particules collisions models and thermodynamic variables, it is known to vary as $D \sim \frac{T^{3/2}}{p}$ [30]. For fluid mechanics problems involving inert gases, a simplified model is usually chosen. D is defined thanks to the Schmidt Number Sc expressing a ratio between viscous and mass diffusions:

$$D = \frac{\mu}{\rho Sc} \tag{21}$$

An usual hypothesis based on experimental observations is to consider Sc constant. As for heat transfer, we furthermore define a turbulent diffusion coefficient to compute $\mathbf{J}_{t_i} = -\rho D_t \nabla Y_i$ the unresolved turbulent mass fluxes. This coefficient is expressed thanks to a turbulent Schmidt number to form the total diffusion coefficient:

$$D_t = \frac{\mu_t}{\rho Sc_t}, \quad D^* = D + D_t \tag{22}$$

Sc and Sc_t are usually defined empirically with wind tunnel experiments and numerical simulations.

3. NUMERICAL METHODS

The previous section concerned the continuous form of the equations associated to thermodynamics of a binary gas mixture. To solve these two-species Navier-Stokes equations, modified numerical schemes are needed. An implicit finite volume formulation of the governing equations (2^{nd} order in time) yields for an hexahedral cell (i,j,k) with a volume Ω_{ijk}:

$$\frac{3}{2}\Delta(\mathbf{w}_c)^{n+1}_{ijk} - \frac{1}{2}\Delta(\mathbf{w}_c)^{n}_{ijk} + \frac{\Delta t}{\Omega_{ijk}}(\mathbf{F}(\mathbf{w}_c) - \mathbf{G}(\mathbf{w}_c))^n_{ijk,l} = -\frac{\Delta t}{\Omega_{ijk}}\sum_{l=1}^{6}\left[\left(\frac{\partial \mathbf{F}(\mathbf{w}_c)}{\partial \mathbf{w}_c} - \frac{\partial \mathbf{G}(\mathbf{w}_c)}{\partial \mathbf{w}_c}\right)^n_{ijk,l}\Delta(\mathbf{w}_c)^{n+1}_{ijk}\right] \tag{23}$$

Where n and n+1 represent consecutive timesteps and $\Delta(\mathbf{w}_c)^{n+1}_{ijk} = (\mathbf{w}_c)^{n+1}_{ijk} - (\mathbf{w}_c)^{n}_{ijk}$. For each interface l (with a normal vector $\mathbf{n}=^t(n_x, n_y, n_z)$ and surface $\Delta S_{ijk,l}$), the discrete convective and diffusive fluxes $\mathbf{F}$ and $\mathbf{G}$ are:

$$\mathbf{F}(\mathbf{w}_c)_{ijk,l} = \begin{pmatrix} \rho_1(\mathbf{V}.\mathbf{n}) \\ \rho_2(\mathbf{V}.\mathbf{n}) \\ \rho u(\mathbf{V}.\mathbf{n}) + pn_x \\ \rho v(\mathbf{V}.\mathbf{n}) + pn_y \\ \rho w(\mathbf{V}.\mathbf{n}) + pn_z \\ (\rho E + p)(\mathbf{V}.\mathbf{n}) \end{pmatrix}_{ijk,l} .\Delta S_{ijk,l} \tag{24}$$

$$\mathbf{G}(\mathbf{w}_c)_{ijk,l} = \begin{pmatrix} \mathbf{J}_1.\mathbf{n} \\ \mathbf{J}_2.\mathbf{n} \\ \tau^*_{xx}n_x + \tau^*_{xy}n_y + \tau^*_{xz}n_z \\ \tau^*_{xy}n_x + \tau^*_{yy}n_y + \tau^*_{yz}n_z \\ \tau^*_{xz}n_x + \tau^*_{yz}n_y + \tau^*_{zz}n_z \\ (\overline{\overline{\tau}}^*.\mathbf{V} - \mathbf{q}^* + \mathbf{J}_E).\mathbf{n} \end{pmatrix}_{ijk,l} .\Delta S_{ijk,l} \tag{25}$$

To solve equation (23), different methods have been enhanced to adapt the FLU3M solver. They are presented here but the details of these features will be described in a future article.

3.1 Discrete fluxes

Explicit convective fluxes A two-species Roe scheme was already available for the evaluation of the explicit convective fluxes for binary gas mixture flows [1], we have adapted two others : AUSM+ [17] a second robust upwind scheme and an AUSM+(P) [19] as a basis for high-fidelity, scale resolving schemes. The spatial accuracy of those schemes are extended thanks to several MUSCL approaches (Minmod (2nd Order) , Koren (3rd Order) and 3rd-Order upwind biased (called Kap here)).

Explicit diffusion fluxes To evaluate the diffusion flux vector G, the average of their right and left center values are used to estimate $\rho, D^*, \mu^*, \lambda^*, \mathbf{V}, h_i$ at the cell interface. Estimations of velocity, mass fraction and temperature gradients are needed as well. To this end, a corrected Green-Gauss mono-species approach described in [18] is adapted to include mass fraction gradient computations. It is designed to prevent numerical instabilities that can arise due to odd-even decoupling oscillations allowed by the original Green-Gauss approach.

Implicit fluxes As seen in equation (23), Jacobian matrices of the fluxes are involved in the implicit formulation of the time scheme. We have assessed these matrices by adapting the procedure presented by Pechier [21] for mono-species flows.

3.2 User's input

In the numerical framework implemented, the user has to define Sutherland's law constants [μ_{0_i},S_i,T_{0_i}] and [γ_i, c_{v_i}, Pr_i] for the two gases (i=1,2) involved in the simulation and [Pr_t, Sc, Sc_t] for the mixture. These quantities permit to initialize the conservative variables ($\rho_1 = \rho * Y_1, \rho_2 = \rho * Y_2, \rho\mathbf{V}, \rho E$) in any zone of the computational domain.

4. TEST CASES

As the method is now presented, results on a set of validation cases of growing complexity are described.

4.1 Shock Tube

Theoretical background The shock tube is a fundamental exercise in gas dynamics as well as a reference case for the numerical resolution of the Euler equations [8]. The analytical solution of this problem can be computed and an evaluation of the numerical results can thus be performed. The studied configuration is presented in

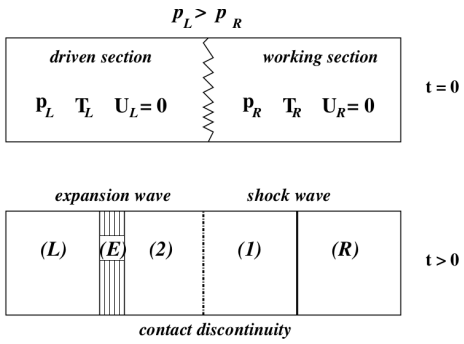

Figure 1: Shock tube configuration [8]

Fig.1. The infinite tube, that can be considered as monodimensional along an abscissa x, is initially divided into two zones (left L, right R) separated by a membrane located at $x = x_0$. The pressure in the left zone is higher than in the right one and both fluids are at rest. We consider a sudden rupture of the membrane at the time t=0. Several phenomena such as expansion and shock waves occur to balance the pressure between the two zones. The analysis of Euler's equations enables to describe analytically the evolution of physical properties in the tube and one can then form a fixed point algorithmic problem to determine the pressure at the contact discontinuity [1][8]. The time and space variations of physical properties can thus be expressed thanks to characteristic curves.

Air shock tube The first test case consists in the simulation of a shock tube with air at both side of the tube. The parameters, chosen to ensure high pressure and density ratios are presented in Tab.1. We consider the tube on a 1 m length (x_0=0.5 m) and study the flow after 0,2 s. The mesh used for the FLU3M calculation is uniform with 500 points along the length of the tube and 10 points in each normal direction.

γ_L	p_L	ρ_L	γ_R	p_R	ρ_R
1.4	$10/\gamma$	8	1.4	$1/\gamma$	1

Table 1: Initial parameters for the air shock tube

During preliminary tests both fluids are defined as air and each zone is initialized with various mass fractions (1/0; 0.7/0.3; 0/1). A binary gas mixture simulation is then performed by defining air as a mixture of nitrogen N_2 (76.7 *mass%*) and oxygen O_2(23.3 *mass%*) as in [14]. The thermodynamic properties were taken from NIST tables ($\gamma_{O_2} = 1.396$ and $\gamma_{N_2} = 1.401$). The simulations were performed with different schemes and a Minmod limiter.

On Fig.2, describing velocity and density variations, one can distinguish the expansion fan, the contact discontinuity and the shock wave along the x axis and verify that the simulation results agrees well with the analytical one. Small differences are due to numerical dissipation which slightly differs between the three schemes, the AUSM$^+$(P) being the less dissipative one.

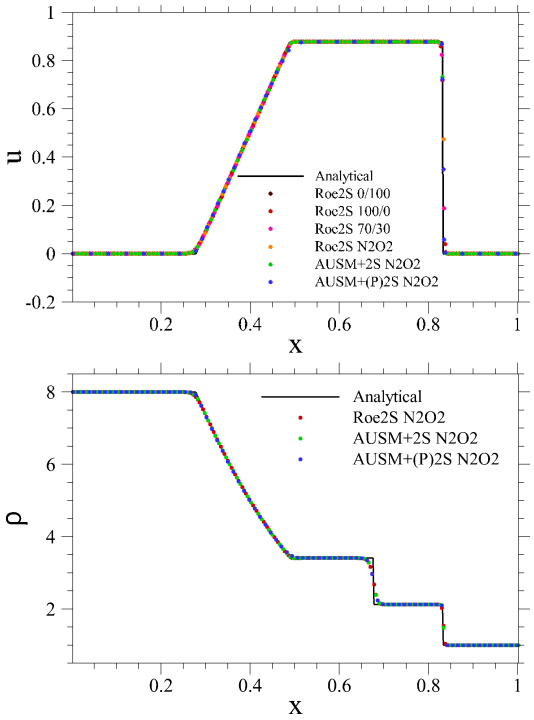

Figure 2: Velocity (top) and density (bottom) distribution in the air shock tube.

Two species shock tube We now consider two different species, with different specific heat ratios. Each species fills one zone of the tube. The parameters chosen (Tab.2) ensure that mass diffusion is inhibited. Several reconstruction methods are tested on this case. Results presented in Fig.3 show again a good agreement with the analytical solution. Furthermore, expected differences between MUSCL reconstruction methods appear. The two 3^{rd} order methods are less dissipative and capture the shock and the contact discontinuity more sharply than with a Minmod limiter. However they tend to induce oscillations near those discontinuities which can cause numerical instabilities. For instance, only Roe's scheme is stable with the upwind 3^{rd} order approach (Kap).

γ_L	p_L	ρ_L	Y_{1_L}	γ_R	p_R	ρ_R	Y_{1_R}
1.4	1	1	1	1.2	0.1	0.125	0

Table 2: Initial parameters for the two species shock tube

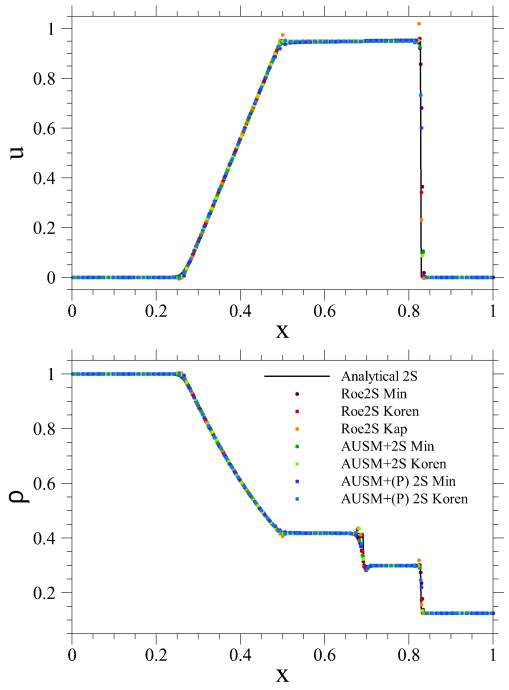

Figure 3: Velocity (top) and density (bottom) distributions in the shock tube containing two gases.

4.2 Supersonic Confluence

Studying the confluence of two supersonic streams as in [2] has two main interests. First, as a 2D version of the shock tube, most of the solution can again be computed analytically. Second, this configuration represents a first step towards the simulation of a supersonic propulsive jet entering a supersonic flow with a different γ, a different velocity and a different pressure (JPR).

Theoretical background As presented on Fig. 4, when two supersonic streams (P_1, M_1, γ_1) and $(P_5 > P_1, M_5, \gamma_5)$, meet at the end of a splitting plate, several phenomena occur to reach a pressure balance. As for an under expanded jet (JPR = $\frac{P_5}{P_1} > 1$), the gas flowing from zone (5) expands to reach a pressure $P_3 = P_2$ and a Mach number M_3. This happens through an expansion fan (5-4-3) delimited by two Mach waves issuing from the trailing edge of the plate with angles $\Psi_1 = -arcsin(\frac{1}{M_5})$ and $\Psi_2 = -arcsin(\frac{1}{M_3}) + \beta$, β being the angle of the contact discontinuity. The deviation of the gas flowing from (1) by the contact discontinuity induces the formation of an oblique shock wave with an angle θ.

The analytical resolution is quite similar to the shock tube case, though the aim here is to determine the different angles of the flow. Using relations from [22] and [2], we have established a fixed point problem giving the value of β, $P_2 = P_3$, M_2 ,M_3, θ , Ψ_1 and Ψ_2.

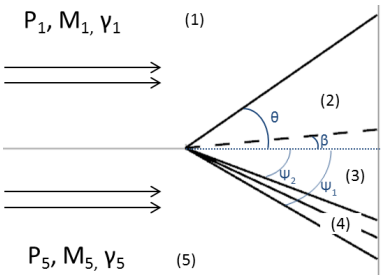

Figure 4: Confluence of two supersonic streams. Shock (1-2), contact discontinuity (2-3), expansion fan (3-4-5).

Air-Argon Test Case A case of the confluence of an air stream (zone (1)) and an argon stream (zone (5)) has been tested. Parameters of the case and analytical results are listed in Tab.3. The mesh size for the simulation is 2x4x0.05 m with 600x2000x2 cells. The splitting plate is modelled with a slip condition and symmetry conditions are imposed on lateral faces. Simulations are performed with the two upwind schemes (Roe2S, AUSM+2S) and the three MUSCL reconstructions.
Mach number distribution are visualized in Fig. 5. One can note a good agreement with the analytical solution for the flow angles and Mach number values in zones (2) and (3) ($M_2 = 1.802 \pm 5.10^{-3}$; $M_3 = 2.277 \pm 5.10^{-3}$). A more quantitative evaluation is presented by plotting the pressure distribution in the normal direction for $x = 0.25m$ on Fig.6. For the sake of clarity, only two representative curves are shown. These results illustrate the good agreement with the analytical solution. Furthermore, as seen on the previous case, small oscillations around discontinuities (contact discontinuity and shock) appear when using a 3rd order MUSCL reconstruction.

γ_1	p_1	M_1	γ_5	p_5	M_5
1.4	1	2	1.669	2	2

M_2	$\frac{p_2}{p_1}$	M_3	β	θ	Ψ_1	Ψ_2
1.802	1.353	2.277	5.5	34.8	-30	-20.5

Table 3: Initial parameters and analytical results

4.3 Pure mass diffusion

Theoretical background The first diffusive case studied is pure mass diffusion. To this end, the same configuration as for the shock tube (Fig 1) is used, but this time all thermodynamic variables (ρ, p, T, **U=0**) are the same in the left and right zones. Thus, the study is here limited

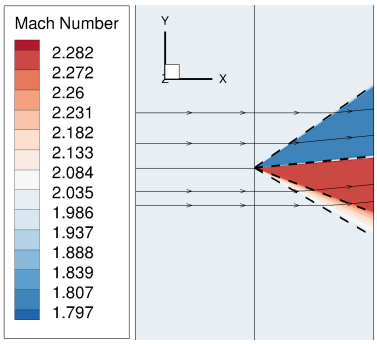

Figure 5: Mach number distribution and streamtraces (Roe2S with Koren). (- -) Analytical deviation.

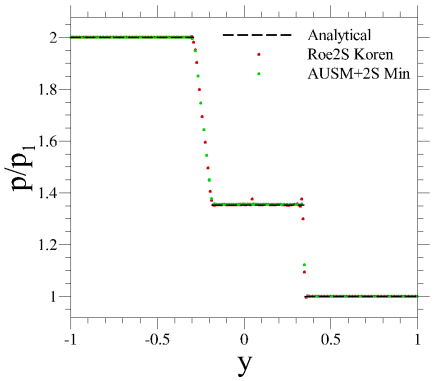

Figure 6: $\frac{p}{p_1}$ distibution along y (x=0.25m)

to mass diffusion between gas 1 (left) and gas 2 (right). Fick's diffusion model is described by a differential equation which solution $Y_1(x,t)$ is in this case [6]:

$$\frac{\partial Y_1}{\partial t} = D\frac{\partial^2 Y_1}{\partial x^2} \rightarrow Y_1(x,t) = \frac{1}{2} erfc(\frac{x}{2\sqrt{Dt}}) \qquad (26)$$

With $erfc(z) = 1 - erf(z)$ the complementary error function. The spatial distribution of Y_1 is self-similar and only depends on the product D*t. We will then evaluate the solver resolution compared to this analytical solution.

Numerical results The results are presented for three different diffusion coefficients D ($\frac{1}{3}$,1, and 3) on Fig.7. Comparison with analytical results is very satisfying and the numerical solution are indeed self-similar.

4.4 Flat Plate Boundary Layer

The flat plate boundary layer is the reference case for wall-bounded flows. We present here a subsonic (M=0.2) and a supersonic (M=2) test cases. The gas is air, defined as a mixture of N_2 and O_2. Results are compared to mono-species RANS and DNS simulations [27]. Only Roe2S and AUSM+2S, usually used for attached boundary layer, are tested. The rectangular computational mesh

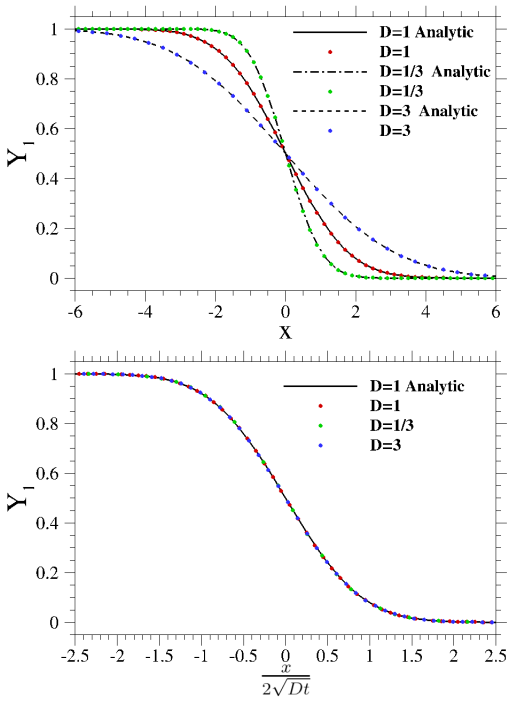

Figure 7: Y_1 spatial variation with different diffusion coefficients and at t=1s (top). Scaled version (bottom).

contains 712x126x2 cells and almost 80 points are clustered in the boundary layer with $\Delta y^+ = 1$.

Subsonic Boundary Layer The computational results for the subsonic boundary layer are shown in Fig.8. A good agreement with empirical laws and RANS mono-species simulations is obtained. RANS (S-A) results fit the DNS results with two known discrepancies, namely an overestimation ($\leq 5\%$) of u^+ in the buffer zone [11] and an underestimation ($\approx 1.4\%$) of u^+ in the outer layer, related to the overestimation of skin friction by the Spalart-Allmaras model [10].

Supersonic Boundary Layer Computational results for the supersonic case are presented in Fig.9 where binary gas mixture u^{+*} profiles (Van Driest transformation) are compared to u^{+*} for an air RANS simulations and dimensionless velocity u^+ from the empirical, RANS and DNS incompressible results. A very good agreement is obtained between air and N_2O_2 supersonic simulations for the two schemes. Comparison with incompressible RANS and empirical solutions is also satisfying.

4.5 Supersonic Mixing Layer

We present here RANS and ZDES bi-species computations of the coaxial jet experiment presented in [7, 5] which was designed for CFD code validation as used in

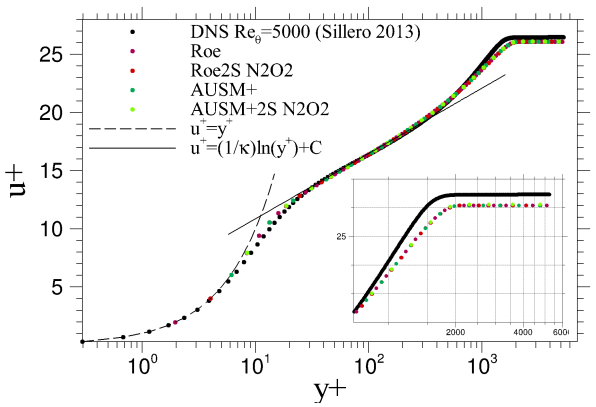

Figure 8: Dimensionless velocity for the subsonic N_2O_2 boundary layer (Re_θ=5000), compared to empirical (κ=0.41, C=5.25), RANS and DNS [27] air results.

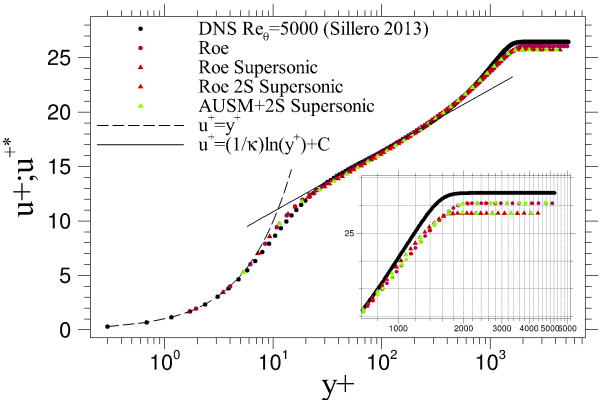

Figure 9: Van Driest velocity u^{+*} for the supersonic N_2O_2 boundary layer (Re_{δ_2}=5000), compared to dimensionless velocity from empirical (κ=0.41, C=5.25), RANS and DNS [27] mono-species results.

[5, 3, 29]. In the version studied here, two co-flowing supersonic jets of argon (center jet) and air (outer jet) discharge in a quiescent atmosphere. The geometry of the coaxial jet structure is showed in Fig.10 with dimensions in mm. The center body contains a supersonic nozzle for the argon jet with an exit diameter D_{center}=10 mm, and the gap between the center and outer bodies creates a supersonic nozzle for the coflow air jet with an exit outer diameter D_{coflow}=60.47 mm. The two nozzles were designed to provide a nominal Mach number of 1.8 at the exit. The jet discharge in a cylindrical plenum filled with air at atmospheric pressure. The initial flow conditions in terms of total pressure (P_{tot}) and total temperature (T_{tot}) are presented in Tab.4. Gas composition probes were used to measure argon mass fraction (Y_{argon}) distributions in several transverse planes from x/D_{center}=0.3 to 45.

The domain for the calculations is extended to 150 center jet diameter (D_{cj}) along the streamwise direction and more than $20D_{cj}$ radially. To cope with the axisymmetric geometry, an O-H grid topology is adopted to avoid a singularity on the axes. The mesh (Fig.11) contains 65M cells with 200 points in the azimuthal direction ($\Delta\theta = 1.8°$). For the RANS computations, the Spalart-Allmaras [28] turbulence model is used and the convective fluxes are computed with an AUSM+ scheme and a Minmod MUSCL reconstruction. For the ZDES computations, the convective fluxes are computed thanks to an hybrid scheme [24] and a Koren MUSCL reconstruction. The timestep for ZDES is $5.10^{-8}s$. We chose to let the flow develop during 6 ms before using another 6 ms period to perform time average. For thermodynamic parameters, Sc between air and argon is set to 0.8 and three Sc_t (1; 0.5 and 0.25) are tested to evaluate the models sensitivity, we thus performed three RANS (R1; R05; R025) and three ZDES (Z1; Z05; Z025) computations.

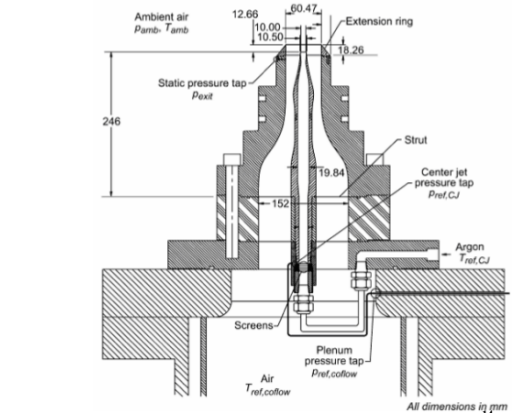

Figure 10: Clifton & Cutler [5] experimental setup.

	Center jet	Coflow jet	Ambient
T_{tot}	297.9(±3.5)	294.3(±3.5)	294.6(±3.5)
P_{tot}	615.86(±5.5)	580.68(±4.4)	101.32(±0.6)

Table 4: Clifton & Cutler [5] initial conditions

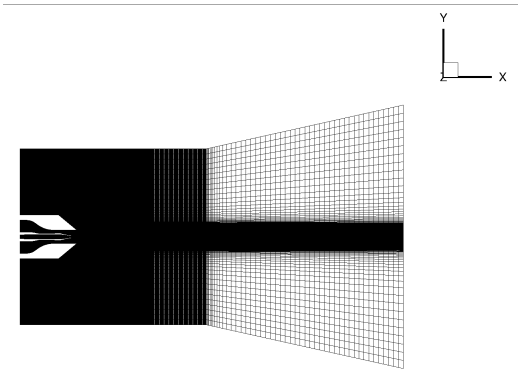

Figure 11: 2D side view of the computational domain

Fig.12 shows the Mach number distribution obtained with

a ZDES simulation, it is very similar to the one obtained in [3] and we verify that both flows reach M=1.8 at the exit of both nozzles. This view enables to distinguish the mixing layer between the center jet (argon) and the coflow jet (air), which is of particular interest here, and the mixing layer between the coflow and the ambient air.

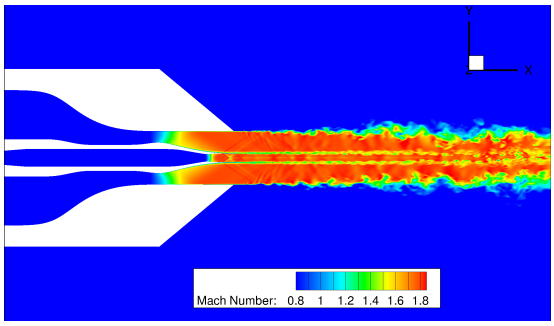

Figure 12: Instantaneous Mach number field (ZDES)

To study the influence of Sc_t on the predicted turbulent mixing, Fig.13 shows an example of a computed mass fraction distribution on which the predicted position of the $Y_{argon} < 0.99$ limit for the six computations and for the experiment have been signalled with bars. The positions obtained with ZDES show a major improvement compared to RANS since they are both closer to the experimental position and less dependent to the value of Sc_t. To confirm these results, examples of the argon mass fraction distribution in transversal planes are shown in Fig.14 for the location X/D=22.1. The strong influence of the value of Sc_t on RANS results observed in [5][3] is confirmed. As expected thanks to the reduced influence of unresolved turbulent fluctuations, the results obtained with ZDES computations appear almost independent of Sc_t. They furthermore provide a good agreement with experimental measurements and locally improve results from previous RANS/LES computations [3, 29].

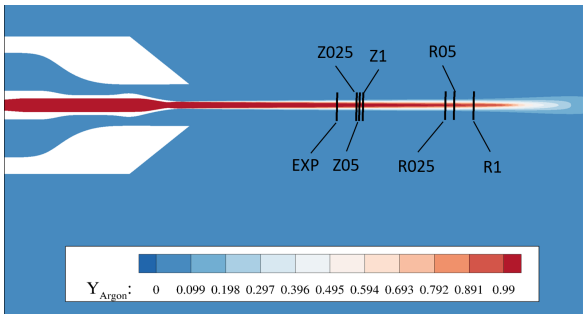

Figure 13: Argon mass fraction (Y_{argon}) distribution and $Y_{argon} < 0.99$ predictions (—).

Overall the results obtained on the several test cases show that the newly developed bi-species numerical framework presented here can be used with confidence to compute compressible turbulent bi-species flows. It has then been applied to a generic space launcher afterbody

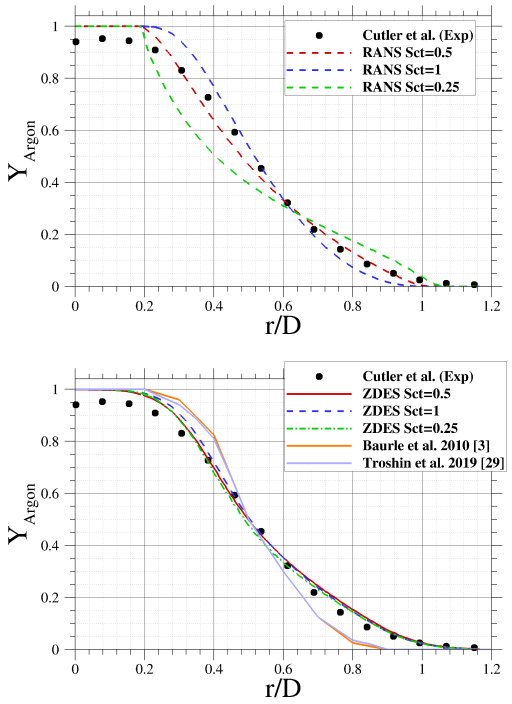

Figure 14: Transversal argon mass fraction (Y_{Argon}) distributions compared to experimental results [5] at X/D=22.1. RANS (top) and ZDES (bottom).

5. SPACE LAUNCHER AFTER-BODY

A two cylinder geometry (Fig. 15), studied experimentally with air as the exhaust gas [12] is our reference case. The ratios d/D=0.4 and L/D=0.6 are representative of usual space launchers. The freestream Mach number is 0.7 and the Nozzle Pressure Ratio (NPR=$\frac{p_t}{p_\infty}$) is ≈34, corresponding to an adapted air jet. Three RANS simulations using respectively air, argon and helium for the propulsive jet are performed in order to study the influence of the jet parameters on the base flow. As the specific heat ratio γ_j and the product R_jT_j(specific gas constant and exit jet temperature) have been experimentally observed as useful parameters [15], their values are shown in Tab.5. The computational mesh, designed for ZDES, contains 16M cells. A ZDES mode 1 simulation is also computed with air as the propulsive gas to assess the improvements in base pressure coefficient Cp_b prediction compared to RANS.

Fig. 16 shows the base flow configuration for the air and helium cases. First, as expected due to a higher value of γ_j, the jet expansion, visualised with the isoline M=1, is smaller for helium than for air. This causes a decrease of the interaction area between the jet and the freestream.

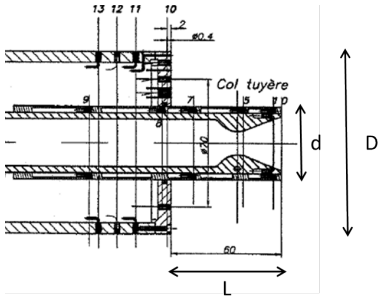

Figure 15: Afterbody model [12] (Lengths in mm)

	Air	Argon	Helium
γ_j	1.4	1.67	1.67
R_jT_j	2.87e+4	1.2e+4	1.04e+5

Table 5: Properties of the different exhaust gas

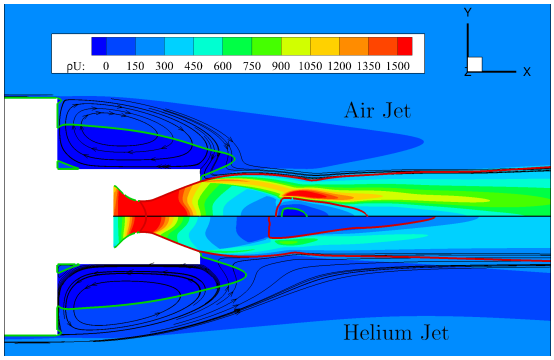

Figure 16: Comparison of the base flow between air and helium jet. — Isoline M=1 — Isoline U=0

Second, the length of the recirculation zone (L_R), visualised with the isoline u=0, is significantly longer with the helium jet ($\frac{L_R}{L} = 1.33$) than for the two other gases, sign of a lower entrainment of the base flow by the jet. A lower jet momentum and a higher convective Mach number in the mixing layer linked to the increase in R_jT_j can explain this result [15]. L_R is slightly longer for the argon jet ($\frac{L_R}{L} = 1.25$) compared to the air jet ($\frac{L_R}{L} = 1.24$), this could be due to a compensation between a smaller jet interaction area due to the increase of γ_j and the decrease in R_jT_j causing an increase the entrainment effect.

Fig. 17 shows the radial variation of Cp_b. Focusing on RANS results, Cp_b is significantly higher with the helium jet than with the two other gases and it is slightly greater with the argon jet compared to the air jet. These results are in coherence with the previous observations, indeed the decrease of the entrainment effect for the helium case is the reason for the observed increase in base pressure [15]. However, the RANS air simulation results compare poorly with experimentally measured Cp_b. RANS models are indeed known to be limited for base flows. The

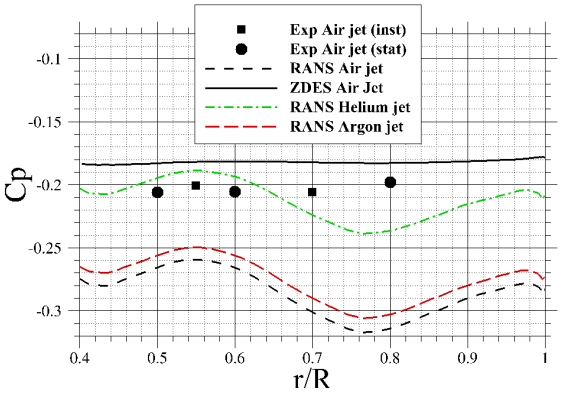

Figure 17: Radial variation of Cp_b. Exp. from [12]

use of ZDES, enabling the resolution of large scale coherent structures involved in the base flow, considerably improves the predictions of pressure levels. In this spirit, instantaneous results using bi-species ZDES mode 1 are shown in Fig.18. This visualisation enables to assume the important role of coherent structures in the mixing process between the jet and the freestream as observed on the supersonic mixing layer case.

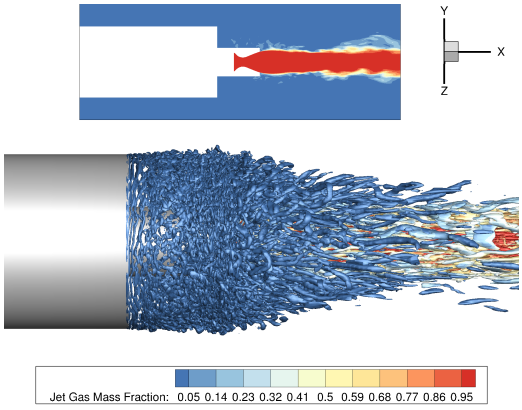

Figure 18: Instantaneous visualisation of a binary gas mixture ZDES : Iso-contours of Q criterion (Q^*D^2/U^2=40) coloured by the jet gas mass fraction.

6. CONCLUSION

This paper presents the extension of a mono-species Navier-Stokes solver to permit the simulation of inert bi-species flows. This extended numerical framework has been validated on a wide range of configurations including a shock tube, a supersonic flow confluence, molecular diffusion, subsonic and supersonic boundary layers and a supersonic mixing layer thanks to comparison of RANS and ZDES computations with analytical, experimental and numerical results from the literature. Used for RANS computations of space launcher base flow, this framework gave results in agreement with known tenden-

cies regarding the influence of the jet properties on base pressure. The observed limitations of RANS models for quantitative predictions however motivates further base flow computations using bi-species ZDES.

REFERENCES

[1] R. Abgrall. Généralisation du schéma de roe pour le calcul d'écoulement de mélanges de gaz à concentrations variables. *La recherche aérospatiale*, (6):31–43, 1988.

[2] S. Arabi, J.-Y. Trépanier, and R. Camarero. A simple extension of roe's scheme for multi-component real gas flows. *Journal of Computational Physics*, 2019.

[3] R. A. Baurle and J. R. Edwards. Hybrid reynolds-averaged/large-eddy simulations of a coaxial supersonic freejet experiment. *AIAA Journal*, 48(3):551–571, mar 2010.

[4] P. Catalano, M. Marini, A. Nicoli, and A. Pizzicaroli. Cfd contribution to the aerodynamic data set of the vega launcher. *Journal of Spacecraft and Rockets*, 44(1):42–51, 2007.

[5] C. W. Clifton and A. D. Cutler. A supersonic argon/air coaxial jet experiment for computational fluid dynamics code validation. 2007.

[6] J. Crank et al. *The mathematics of diffusion*. Oxford university press, 1979.

[7] A. D. Cutler, G. S. Diskin, J. P. Drummond, and J. A. White. Supersonic coaxial jet experiment for computational fluid dynamics code validation. *AIAA journal*, 44(3):585–592, 2006.

[8] I. Danaila, P. Joly, S. M. Kaber, and M. Postel, editors. *Gas Dynamics: The Riemann Problem and Discontinuous Solutions: Application to the Shock Tube Problem*, pages 213–233. Springer New York, New York, NY, 2007.

[9] S. Deck. Recent improvements in the Zonal Detached Eddy Simulation (ZDES) formulation. *Theoretical and Computational Fluid Dynamics*, 26(6):523–550, Oct. 2011.

[10] S. Deck, N. Renard, R. Laraufie, and P.-É. Weiss. Large-scale contribution to mean wall shear stress in high-reynolds-number flat-plate boundary layers up to 13650. *Journal of Fluid Mechanics*, 743:202–248, Mar. 2014.

[11] S. Deck, P.-É. Weiss, M. Pamiès, and E. Garnier. Zonal detached eddy simulation of a spatially developing flat plate turbulent boundary layer. *Computers & Fluids*, 48(1):1–15, Sept. 2011.

[12] D. Deprés. *Analyse physique et modélisation des instationnarités dans les écoulements d'arrière-corps transsoniques*. PhD thesis, Aix-Marseille 2, 2003.

[13] M. Dormieux, P. Guillen, and R. Abgrall. Numerical simulation of transverse jet flows by a nonreactive two species multidomain euler flow solver. In *28th Aerospace Sciences Meeting*, page 126, 1990.

[14] P. J. M. Ferrer, R. Buttay, G. Lehnasch, and A. Mura. A detailed verification procedure for compressible reactive multicomponent navier–stokes solvers. *Computers & Fluids*, 89:88–110, jan 2014.

[15] W. E. Hammond. *Design Methodologies for Space Transportation Systems*. American Institute of Aeronautics and Astronautics, jan 2001.

[16] J. O. Hirschfelder, C. F. Curtiss, R. B. Bird, and M. G. Mayer. *Molecular theory of gases and liquids*, volume 165. Wiley New York, 1964.

[17] M.-S. Liou. A sequel to AUSM: AUSM+. *Journal of Computational Physics*, 129(2):364–382, Dec. 1996.

[18] L. Manueco, P.-É. Weiss, and S. Deck. On the coupling of wall-model immersed boundary conditions and curvilinear body-fitted grids for the simulation of complex geometries. *Computers and Fluids (in revision)*, 2020.

[19] I. Mary and P. Sagaut. Large Eddy Simulation of Flow Around an Airfoil Near Stall. *AIAA Journal*, 40(6):1139–1145, June 2002.

[20] R. Pain, P.-E. Weiss, and S. Deck. Zonal Detached Eddy Simulation of theFlow Around a Simplified Launcher Afterbody. *AIAA Journal*, 52(9):1967–1979, Sept. 2014.

[21] M. Pechier. *Prévisions numériques de l'effet Magnus pour des configurations de munitions*. PhD thesis, Poitiers, 1999.

[22] M. Pindzola. Jet simulation in ground test facilities. Technical report, Advisory Group for Aeronautical Research and Develoment Paris (France), 1963.

[23] T. Poinsot and D. Veynante. *Theoretical and Numerical Combustion*. R.T. Edwards Inc., 2005.

[24] J. Reynaud, P. Weiss, and S. Deck. Numerical workflow for scale-resolving computations of space launcher afterbody flows with and without jets. *Computers and Fluids*, 2021.

[25] D. Saile, D. Kirchheck, A. Gülhan, C. Serhan, and V. Hannemann. Design of a gh2/gox combustion chamber for the hot plume interaction experiments at dlr cologne. In *8th European Symposium on Aerothermodynamics for Space Vehicles*, 2015.

[26] B. Sainte-Rose. *Simulations numériques d'écoulements réactifs massivement décollés par une approche hybride RANS/LES*. PhD thesis, Châtenay-Malabry, Ecole centrale de Paris, 2010.

[27] J. A. Sillero, J. Jiménez, and R. D. Moser. One-point statistics for turbulent wall-bounded flows at reynolds numbers up to $\delta+ = 2000$. *Physics of Fluids*, 25(10):105102, 2013.

[28] P. Spalart and S. Allmaras. A one-equation turbulence model for aerodynamic flows. In *30th Aerospace Sciences Meeting and Exhibit*. American Institute of Aeronautics and Astronautics, Jan. 1992.

[29] A. Troshin, A. Shiryaeva, V. Vlasenko, and V. Sabelnikov. Large-eddy simulation of helium and argon supersonic jets in supersonic air co-flow. In *Progress in Turbulence VIII. iTi 2018. Springer Proceedings in Physics*, volume 226, pages 253–258. Springer International Publishing, 2019.

[30] F. A. Williams. *Combustion theory*. CRC Press, 2018.